Bioinspired fibrillar adhesives: a review of analytical models and experimental evidence for adhesion enhancement by surface patterns.

R. D. O'Rorke[1], T. W. J. Steele[1†*], and H. K. Taylor[2††*]
[1] School of Materials Science and Engineering,
Nanyang Technological University, Singapore.
[2] Department of Mechanical Engineering,
6159 Etcheverry Hall,
University of California, Berkeley, CA 94720 U.S.A.

† wjsteele@ntu.edu.sg
†† hkt@berkeley.edu
* Corresponding authors

September 9, 2015

For publication in the Journal of Adhesion Science and Technology

Abstract

Fibrillar structures are found on the attachment pads of insects and small reptiles. These structures enable exquisite conformation to rough surfaces, increase the number of van der Waals interactions between the structure and the target surface, and thus enhance adhesion. Biomimetic adhesives replicate this effect by patterning polymer films with micron- or sub-micron-sized protrusions. Numerical contact-mechanics models as well as experimental adhesion measurements have been reported for a variety of protrusion shapes including flat, rounded, mushroom and spatula geometries. Although superior adhesion has been reported for the mushroom and spatula tip geometries, straight, flat-tipped pillars offer the potential for much simpler mass-production such as by injection moulding and are thus the focus of this review.

Existing models for straight, flat-tipped pillar arrays do not fully agree with reported experimental results. Analytical models are generally limited to elastic materials, and inherently assume that neighbouring pillars behave independently. For elastic pillars in close proximity, however, pillars do in fact interact mechanically, affecting adhesion. Moreover, visco- and hyper-elastic materials are often used in practice, yet dissipative effects receive little attention in analytical models. We find that no study has conclusively investigated the limit of adhesive strength achievable by fibrillar adhesives. It also remains unclear what happens to the adhesive strength as the areal density of contacting regions approaches 100%.

Keywords: *Adhesive, bioadhesive, biomimetic, contact mechanics, gecko*

1 Introduction

Fibrillar structures are found throughout nature on the attachment pads of insects, spiders, and lizards, allowing both strong adhesion and easy release for locomotion [5, 9, 60, 61]. The very high aspect ratios of these setae (> 20) allow exquisite conformation to rough surfaces, since the individual setae can deform more easily than a continuous surface, giving rise to larger contact areas than would otherwise be possible. Such is the increase in contact area that loads from μg (flies) to 100 g (lizards) can be supported by van der Waals interactions [5]. Fibrillar structures can give rise to strong adhesion for high-Young's-modulus materials, such as beta-keratin in gecko setae which has a Young's modulus of 1.6 GPa [58].

Considerable effort has been invested in developing biomimetic polymer adhesives patterned with pillar arrays of various geometries. Although both friction and adhesion are important in gecko climbing and locomotion [6], most research has focused on fibrillar surfaces for adhesion. Setae geometry is complex and hierarchical in nature, with spatula structures and mushroom, or suction-cup, structures common [25]. Hierarchical geometries are difficult to replicate in synthetic adhesives, and efforts tend to be focused on low aspect ratio (<5) pillars with flat [3, 27, 39, 45–47, 52], rounded [27, 38], spatula [27, 32] or mushroom [25, 27, 41] tips.

Analytical models of fibrillar adhesion have been adapted from the contact mechanics models of Johnson, Kendall and Roberts [36, 37]. A major feature of these analytical models is that the adhesive strength of a single pillar (the adhesive force per unit contact area) increases as pillar diameter decreases, giving rise to an anticipated increase in adhesion beyond increased contact area [5]. A primary research goal is to elucidate the effects of pillar geometry and density on adhesion, which is still not fully understood. Furthermore, testing protocols, substrates, and pillar geometries vary greatly between studies, making direct comparison of reported data difficult.

There are several excellent reviews of gecko adhesion models [8, 40, 79]. These reviews focus on gecko adhesion and locomotion, giving less attention to synthetic gecko adhesives, which is the focus of this review. Here, we examine analytical models of fibrillar adhesion, discuss

the contact mechanics principles on which they are based, and review reported data on fibrillar adhesives. Whilst we briefly discuss tilted pillars and pillars with spatula and mushroom tips, this review focuses on straight, flat-tipped pillars because of the relative ease with which these simple geometries could be produced using standard manufacturing processes, such as injection moulding [78]. We keep in mind three questions: (1) do the analytical models provide an accurate approximation to fibrillar adhesives? (2) do fibrillar structures actually enhance adhesion? and (3) how does pillar geometry influence adhesion?

We begin by discussing two fundamental theories of contact mechanics: the Johnson-Kendall-Roberts (JKR) model [33] and the Derjaguin-Muller-Toporov (DMT) model [20], followed by applications of JKR theory to fibrillar adhesives [5, 31, 62, 66, 73].

2 Analytical models of adhesion

Table 1 near here.

In this section we discuss the complementary JKR and DMT models of contact mechanics, the circumstances in which each model applies and the analytical models of fibrillar adhesion that have been developed from JKR theory. There is a key difference between JKR and DMT theories, in that JKR considers surface forces only in the contact area between two spheres, whereas DMT also considers the surface forces in a region surrounding the contact area. Both JKR and DMT theories are developments of the earlier Hertz theory of contact between elastic spheres, and are illustrated in Figure 1.

2.1 *Hertz, JKR and DMT Theory*

Figure 1 near here

The theories put forward by Johnson *et al.* [33] and Kendall [36, 37] in the 1970's remain the standard theories for interpretation of adhesion test data to date. Hertz theory provides a model of contact between two elastic spheres as a function of a compressive load, P, and does

not consider adhesive forces. Johnson, Kendall and Roberts later considered attractive surface forces [33, 36, 37].

In both JKR and DMT theories adhesion arises from the surface energies of the two spheres. Surface energy is defined as the energy required to create unit area of new surface and can account for hydrophobic interactions, van der Waals forces, hydrogen bonding, covalent bonding, *etc.*. The applicability of JKR and DMT theories has been investigated in depth [34, 48, 50, 67, 70], and the appropriate model can be determined by a single dimensionless parameter [34]:

$$\left(\frac{R^* W^2}{E^{*2} z_0^2}\right)^{1/3} << 1 \qquad \text{for DMT ,} \tag{1}$$

$$\left(\frac{R^* W^2}{E^{*2} z_0^2}\right)^{1/3} >> 1 \qquad \text{for JKR ,} \tag{2}$$

where W is the work of adhesion and z_0 is the equilibrium spacing between atomic planes of the contacting spheres in the Lennard-Jones potential. R^* and E^* are the reduced radius and Young's modulus, respectively, given by:

$$R^* = \frac{R_1 R_2}{R_1 + R_2} \qquad , \tag{3}$$

$$E^* = \left(\frac{1-\nu_1^2}{E_1} + \frac{1-\nu_2^2}{E_2}\right)^{-1} \qquad , \tag{4}$$

where E and ν are the Young's modulus and Poisson's ratio and the subscripts 1 and 2 refer to the two spheres. The anticipated relationships between compressive load, P, displacement, δ, contact radius at zero load, a_0, and adhesive force, F, predicted by Hertz, JKR and DMT theories are summarised in Table 2, where γ is the surface energy, and K, is given by:

$$K = \frac{4}{3} E^* \ . \tag{5}$$

Table 2 near here.

Figure 2 near here.

2.2 *Specific applications of JKR theory*

Kendal applied JKR theory to several specific cases: (a) the flat end of a rigid punch in contact with an elastic half-space under normal loading; (b) a thin elastic layer between the flat end of a rigid punch and a flat rigid substrate under normal loading, and; (c) a thin elastic film being peeled from a flat rigid substrate, as illustrated in Figure 2.

For the case of a rigid punch on an elastic half-space, the derivation can be found in Appendix A, and the adhesive force, F, is given by:

$$F = \sqrt{8\pi E^* \gamma R^3} \ . \tag{6}$$

For the case of an elastic film between a rigid punch and a rigid half-space the derivation can be found in Appendix B, and the adhesive force, F, is given by

$$F = \pi R^2 \sqrt{\frac{2E\gamma}{3t\left(1-2\nu\right)}} \ , \tag{7}$$

where t is the film thickness. Finally, for the case of peeling a thin elastic film from a rigid substrate the derivation can be found in Appendix C, and the adhesive force, F, is given by

$$F = btE\left[\left(\cos\theta - 1\right) + \sqrt{\left(1-\cos\theta\right)^2 + \frac{4\gamma}{2tE}}\right] \ . \tag{8}$$

Kendall verified Equations 6 and 7 by separating an acrylic punch from both a gelatine block and a gelatine film [36], and Equation 8 by peeling a thin gelatine sheet from a glass substrate [37]. The elastic strain energy in the peeled film was negligible for peel angles above 60° and the surface energy dominated. For peel angles below 60° the elastic strain energy dominated.

Yang *et al.* independently derived relationships for the adhesive force for an elastic film between a rigid punch and a flat rigid substrate [76]. The elastic film behaved as a half-space if the film thickness, t, was more than double the punch radius, R, and Equation 6 applied. For film thickness smaller than one-tenth of the punch radius, the following relationships were derived for different boundary conditions at the substrate/film/punch interfaces:

$$F = \pi R^2 \sqrt{\frac{8\mu\gamma}{t}} \qquad \text{for slip at both boundaries;} \tag{9}$$

$$F = \frac{\pi R^3}{2t} \sqrt{\frac{3\mu\gamma}{2t}} \qquad \text{for slip at one boundary;} \tag{10}$$

$$F = \frac{\pi R^3}{t} \sqrt{\frac{3\mu\gamma}{2t}} \qquad \text{for stick at both boundaries,} \tag{11}$$

where the shear modulus, μ, is given by:

$$\mu = \frac{E}{2\,(1+\nu)} \ . \tag{12}$$

This model has not been experimentally verified, and Equation 9, for stick at both boundaries, is not consistent with Kendal's equivalent model, Equation 7.

2.3 *Contact-splitting theory*

Arzt *et al.* determined the adhesive force for an array of pillars with convex tips using JKR theory, in what has become known as contact-splitting theory [5]. This theory was originally presented to describe the scaling of setae density with mass in insects and lizards [5]. However, this has since been discredited by Peattie, who found no correlation between setae density and body mass in a larger study [57]. Nonetheless, contact splitting theory gives an interesting insight into how the size and number of pillars in an array can influence adhesion, as we will now discuss.

A convex-ended pillar of radius R_0 is divided into an array of n convex-ended pillars of radius

R, where $R = \frac{R_0}{\sqrt{n}}$ (i.e. the cross-sectional area of the pillar array is equal to that of the starting pillar), as illustrated in Figure 3. The radius of curvature of the convex tips can be equal to R (self-similar scaling), or equal to R_0 (curvature invariance). The adhesive force, F_T, for the array of pillars, relative to that for a single pillar, F_0, is given by:

$$F_T = n^q F_0 \ , \tag{13}$$

where $q = 0.5$ for self-similar scaling and $q = 1$ for curvature invariance. The derivation of F_T for curvature invariance and self-similar scaling is provided in Appendix D. Spolenak *et al.* independently investigated contact splitting and derived the same relationship as Arzt for curvature invariance and self-similar scaling [68]. Spolenak also considered a flat punch, for which $q = 0.25$.

Figure 3 near here.

The effect of the contact splitting on adhesive force can be understood by considering the contact area for each case [75]. The contact radius at zero load (given by JKR theory) depends on the radius of the pillar tip, which does not change for curvature-invariance, meaning the contact radius scales with n, and the increase in adhesive force is trivial. For self-similar scaling, however, the contact radius at zero load scales with $n^{\frac{2}{3}}$, slightly faster than adhesive force, which scales with $n^{0.5}$. In other words, contact splitting for rounded pillars offers no benefit over using a larger single contact for curvature invariance and is actually disadvantageous for self-similar scaling. For a flat punch the contact area must scale with the density of contacts, or areal density, after contact splitting, as shown experimentally by Varenberg [75].

To achieve a larger contact area a larger preload is required. The relationship between preload and contact area is given by [36]:

$$a^3 = \frac{RP}{K} \ . \tag{14}$$

By equating Equation 14 with the JKR contact radius at zero load, a_0, (see Table 2), it is easy to

see that the preload has the same scaling with n as adhesive force for both curvature invariance and self-similar scaling.

2.4 *Contact-splitting using a cohesive-zone model*

Tang *et al.* independently investigated the contact-splitting phenomenon for a rigid punch using a cohesive zone model [73]. The concept of a cohesive zone has been discussed extensively in relation to fracture mechanics [4, 7, 21]. The cohesive zone is a region of length l immediately outside of the contact area where two surfaces are separated by a distance, δ, but remain held by adhesive forces, as illustrated in Figure 4. Once separated by a critical distance, δ_c, the surfaces separate [73]. Tang investigated the limits of $R \approx l_c$ where the cohesive zone occupies most of the contact area, and $R >> l_c$ where the cohesive zone occupies only a small amount of the contact area. The adhesive strength, σ, was found to be

$$\sigma = \sigma_0 B \chi^{-\lambda} \ , \tag{15}$$

where B and λ are constants and χ is given by

$$\chi = \frac{\sigma_0^2 R}{2\pi E^* W} \equiv \frac{\sigma_0 R}{2\pi E^* \delta_c} \ . \tag{16}$$

The theoretical maximum adhesive strength, σ_0 is a material property estimated to be $\frac{E}{10}$. In the limit of $R \approx l_c$, $\chi << 1$ and the adhesion is flaw-insensitive. In the limit $R >> l_c$, $\chi >> 1$ and adhesion is flaw-sensitive. Tang verified this model by finite element modelling and found $\lambda = 0.4$.

Figure 4 near here.

If we take Tang's value of λ, we can calculate the scaling of adhesive force with n (see Equation 13), and find that $q = 1.6$. This is significantly larger than Spolenak's prediction of $q = 0.25$.

2.5 *Peel zone model of a thin elastic film*

Similarly, Pesika *et al.* modified Kendall's peeling model (Equation 8) to include the region immediately outside the contact area where the adhesive is deformed to produce cavities, yet remains adhered to the substrate, which they called the peel zone [62]. Pesika assumed that the elastic film has a sufficiently high modulus that elastic strain in the film can be neglected and Equation 8 can be approximated by F_{surf} (see Appendix C). The peeling force, F, is given by:

$$F = \left(\frac{\theta}{\theta_0}\right)\left(\frac{1-\cos\theta_0}{\sin\theta}\right)F_{surf} \ , \tag{17}$$

where

$$F_{surf} = \frac{b\gamma}{1-\cos\theta} \ , \tag{18}$$

and θ_0 is the angle between the film and the substrate at the edge of the peeling zone. Equation 17 was shown to accurately model the peeling force of double-sided adhesive tape when peeled from borosilicate glass at peeling angles from 30–90° [62].

Zhou *et al.* later considered the effect of peeling velocity, and found that the peeling force followed a power law relationship with peeling velocity [81]. Zhou also developed a design map for fibrillar adhesives that allow high normal adhesive loads and low peeling strength for easy removal [80]. Zhou found that high peeling strength favours small radius, high aspect ratio pillars with low Young's modulus and thick backing layers [80]. Comparison with Equation 8 shows that pillars reduce the peeling strength dramatically for thin backing layers, whilst the peeling strength converges with Equation 8 for thick backing layers [80]. However, there has been no experimental verification of Zhou's model, and high aspect-ratio pillars are prone to collapsing into clumps of pillars, which is detrimental to adhesion [1].

2.6 *Spring Contact Theory*

Contact-splitting theory inherently assumes that each fibre in an array experiences an identical stress, which is not applicable when considering adhesion to spherical substrates, which are used widely in adhesion testing. When spherical substrates are used the stress on each fibre varies significantly across the contact area from tensile at the perimeter to compressive in the centre. Spring contact theory treats each pillar as a linear elastic spring and there must be zero net strain across the array of springs at zero applied load, as illustrated in Figure 5 [66].

Figure 5 near here.

As the sphere is separated from the adhesive, the outer springs extend to a maximum length, l_{max}, where the strain energy equals the work of fracture of the interface, and the outer springs detach, reducing the contact area whilst the central springs remain compressed. When a critical contact radius, a_{crit}, is reached, the remaining springs cannot support the load and detach simultaneously. The critical contact radius, a_{crit}, is given by:

$$a_{crit} = \sqrt{2R_{probe}\left(l_{max} - l_0\right)} \ . \tag{19}$$

Spring contact theory also provides a model for pressure sensitive adhesion, since the number of springs in contact with the sphere is dependent on the preload. The preload-dependent pull-off force, F_P, is given by:

$$F = 2\sqrt{(F_{max}P)} - P \qquad \text{if } \ a \leq a_{crit} \ , \tag{20}$$

$$F_{max} = \frac{\pi E}{4R_{probe}l_0}a_{crit}^4 \qquad \text{if } \ a \geq a_{crit} \ , \tag{21}$$

where l_0 is the equilibrium spring length (analogous to pillar height), P is the preload, a is the contact radius, and R_{probe} is the radius of the sphere. F_{max} occurs when the maximum contact area at zero load for the array of springs is reached. The Young's modulus of the spring array is given by:

$$E = \frac{l_0 k}{A_0} \ , \tag{22}$$

where k is the spring constant and A_0 is the area of contact above each spring. This model has been shown to accurately describe previously reported experimental data by fitting the value of F_{max} [66].

2.7 *Buckling analysis*

As we have seen, higher preloads are required to bring fibrillar arrays into contact than for a single, continuous contact. However, increasing the preload will eventually lead to buckling of the fibres. Whilst this may be required for conformation to rough substrates, it can be detrimental to adhesion against flat substrates. The critical stress at which buckling occurs, σ_{buckle}, has been investigated for an array of pillars by Jagota *et al.* [31], and is given by

$$\sigma_{buckle} = E\rho\frac{\pi^2}{3}\left(\frac{1}{\alpha}\right)^2 \ , \tag{23}$$

where α is the aspect ratio and ρ is the areal density of pillars. Equation 23 is consistent with buckling criteria for patterned elastomeric stamps [29]. Nadermann has shown that shearing reduces the critical buckling stress [51].

2.8 *Energy dissipation in fibrillar structures under peel*

In a purely elastic system, the work of adhesion is determined by the surface energies at the interface. In reality, adhesive materials may be dissipative, which can serve to increase the work of adhesion and adhesive force as a function of the time-scale of separation.

Jagota *et al.* considered this problem and speculated that all strain energy stored in an array of pillars is dissipated upon separation [31]. The work of adhesion, W, per unit area for a patterned surface is given by

$$W = W_0 + \frac{\rho\gamma^2 h}{2E} \ , \tag{24}$$

where W_0 is the work of adhesion per unit area for a non-patterned surface. Although not stated by Jagota, the surface energy inherent in W_0 should also by multiplied by the areal density, ρ, to account for the reduced surface area of fibrils in contact with a flat substrate. In support of Equation 24, Jagota points out that a fracture energy for rubber larger than the thermodynamic work of adhesion has been reported and attributed to energy dissipation along polymer chains [43, 44].

2.9 *Summary*

The analytical models of adhesion presented focus on specific geometries and configurations that represent only a small number of the likely practical scenarios. For example, peeling a rigid film from an elastic half-space would better approximate the removal of a bioadhesive film; multi-layered films of different Young's moduli would be appropriate for pressure-sensitive adhesives, and; elastic pillars in contact with a rigid substrate would be appropriate for the majority of reported fibrillar adhesives, which will be discussed in the subsequent section.

Nonetheless, these analytical models provide a starting point for the design and interpretation of fibrillar adhesives. On the one hand, contact splitting tells us that an increasing number of sub-contacts allow for larger contact areas and, thus, increased adhesive forces. Spring contact theory also tells us that taller, thinner fibres offer improved adhesive force. On the other hand, fibrillar geometries require a larger preload to establish contact. Dense arrays of high aspect ratio, small radius pillars are prone to *condensation*, where neighbouring pillars collapse into one another. A useful model of pillar condensation was developed by Ahmadi *et al.* [1].

In the following section we discuss the experimental evidence of fibrillar adhesives in the context of the analytical models. We only include work that directly compares the adhesion of fibrillar and non-patterned adhesives, where the effect of fibrillar geometry on adhesion is investigated.

3 Review of experimental data

Fibrillar structures can benefit adhesion in two ways: (1) through improved compliance, and (2) increased adhesive strength. The following review of experimental data aims to answer several questions: (1) is there convincing evidence for adhesion enhancement in using fibrillar arrays? (2) what are the practical limitations on pillar geometry and density? and (3) what role does energy dissipation play in adhesion of fibrillar structures? Where possible we refer to the relative adhesive force and strength, which is the ratio of adhesive forces or strengths for a patterned and non-patterned adhesive.

Reported adhesive forces and strengths are summarised for a range of loading conditions and pillar geometries in Table 4 and Table 5. The relative adhesive forces from numerous studies are plotted as a function of geometrical parameters in Figure 6.

Figure 6 near here.

3.1 *Choice of adhesion test*

Fibrillar adhesives are usually tested under normal loading conditions [3, 10, 23, 27, 39, 46, 52, 54, 72, 74], although peel adhesion [25, 41, 45, 56] and shear adhesion [32, 38, 47] have been reported. This preference likely arises from the application of analytical models to normal loading and peeling. The effect of pillar geometry on adhesion is markedly different for out-of-plane loading (normal and peel) than in-plane loading (shear), as we discuss later.

For perfectly flat substrates and uniform, flat-ended pillars, the adhesive force is largely independent of preload [25, 39, 54]. The exception to this is when fibres are not perpendicular to the surface, resulting in a misalignment of the loading direction, causing preload dependence [16, 39, 59]. For curved substrates, adhesion is preload dependent, or pressure-sensitive [3, 13, 16, 27, 39, 59].

3.2 *Effect of material properties on adhesion*

High Young's-modulus materials are expected to be beneficial for adhesives, since JKR theory predicts that adhesive force scales with $\sqrt{E}$. By far the most popular choice of material for exploration of contact-splitting is polydimethylsiloxane (PDMS), prepared at a 10:1 volume ratio of elastomer to cross-linker with a Young's modulus of several MPa [10, 14, 19, 23, 27, 38, 39, 41, 45, 54, 56, 65, 69, 72]. Poly (vinyl siloxane) (PVS) is also used, and has similar elastic properties to PDMS [24, 25, 59]. With moduli in the GPa range, polyethylene (PE) [52] and polypropylene (PP) [46] have been reported. Some studies utilise polyurethene (PU) with Young's moduli of 55–1200 kPa [17], and several MPa [16]. The choice of material depends largely on the fabrication process, which is the focus of a previous review by Sameoto *et al.* [64].

Figure 7 near here.

Castellanos found that adhesive force increased with increasing Young's modulus for low-Young's-modulus epoxy resins [13], consistent with expectations from analytical models. In contrast, several studies have shown that adhesive force increases with decreasing Young's modulus for rough surfaces and both flat [17] and patterned [63] adhesives, and for patterned adhesives of smooth, curved surfaces [26],

In a perfectly elastic system the choice of material will not affect the relative adhesive force. In reality, however, it is possible that fibrillar structures lead to some energy dissipation during detachment, which will give rise to a positive effect of Young's modulus on relative adhesive force and strength. The reported materials span a five-orders-of-magnitude range of moduli and a range of damping factors, making direct comparison of adhesion difficult. This problem is compounded by the fact that many studies do not report the material properties.

3.3 *Effects of fibre geometry on adhesion*

Small radius, high aspect ratio pillars give better adhesion.

Greiner *et al.* reported the adhesion of PDMS films patterned with pillars to a 5-mm-diameter sapphire sphere, separated at 1 μm s^{-1} following preloads up to 4 mN [27]. Pillar radii from 1–25 μm, heights from 2.5–80 μm, and an areal density of 20% were investigated. Adhesive force was found to be inversely proportional to pillar radius and directly proportional to aspect ratio. The scaling of adhesive force with radius was comparable to the theoretical predictions of Spolenak's contact-splitting theory [68]. For an aspect ratio of one and a pillar radius of 2.5 μm Greiner reported an adhesive force of 1.2 mN, exceeding that for a non-patterned adhesive of 0.8 mN. For a radius of 5 μm the adhesive force was comparable to the non-patterned adhesive, and for a radius of 25 μm the adhesive force was 0.6 mN. Increasing the aspect ratio to four increased the adhesive force to 1.3 mN for a pillar radius of 5 μm. In a separate study, the same group reported that rounding the top edges of the pillars reduced the adhesive force from 1.2 mN to 0.8 mN for a pillar radius of 2.5 μm and aspect ratio of one, all other things constant [19]. This is not surprising, since tip-rounding will reduce the contact area at a given preload and effectively introduce a crack at the edge of the contact area, facilitating detachment.

Atomic force microscopy (AFM) has been used to measure the adhesion of PP pillars to a 30-μm-diameter glass sphere [46]. PP films with a thickness of 1 mm were patterned with 30-μm-high pillars with diameters from 50 nm–5 μm. The adhesive force for 100-nm-diameter pillars with areal density of 15.7% was 350 nN, approximately 30% larger than the 270 nN reported for non-patterned PP. Adhesive force increased with decreasing pillar diameter, with adhesive forces of 150 nN and 100 nN for 5- and 14-μm-diameter pillars, respectively, with an areal density of 30%. A separate study found no significant difference in adhesive force between non-patterned PP and PP patterned with 600-nm-diameter pillars with aspect ratio of 50 and an areal density of 17% [52].

Lambet *et al.* took a unique approach to peel adhesion by fabricating a single PDMS adhesive with adjacent flat and patterned regions, and observed the change in peeling load between the two regions against adhesive tape [45]. The PDMS was patterned with 2-μm-diameter pillars with aspect ratio of 0.35 and areal density of 17%. A preload of 50 kPa was applied for 24 hours, and peeling was conducted at 6 μm s^{-1} normal to the surface. The peeling load for the patterned region was found to be 120 mN, compared to 60 mN for the non-patterned region.

The sample width was not disclosed, which precludes analysis of the peeling strength. To account for penetration of adhesive tape between the pillars, the pillar array was estimated to increase the surface area by a factor of 1.3. The measured adhesive force ratio of two was attributed to a combination of increased contact area and increased adhesive strength. Larger separation rates, higher aspect ratios, and larger areal densities yielded larger adhesive force ratios, consistent with normal loading observations. In contrast, Aksak reported that the normal detachment load for a single PU fibre, radius of 0.75 mm with lengths from 0.16–3 mm, from flat glass decreased with increasing aspect ratio [2].

Higher separation rates give larger adhesive forces.

In contrast to Greiner [27], Kroner reported a loss of adhesion for PDMS patterned with pillars of radius 4.7 μm, aspect ratios 0.2 and 1.95, and areal density of 20%, using a 5-mm-diameter glass sphere separated at 5 μm s^{-1} following a 2 mN preload [39]. The adhesive forces for aspect ratios 0.2 and 1.95 were 1 mN and 1.2 mN, respectively, compared to 4.5 mN for non-patterned PDMS. The discrepancies between the adhesive force ratios reported by Kroner and Griener may arise from the increased separation rate used by Kroner, which can increase energy dissipation, as found with micro-contact printing using PDMS [15, 77]. PDMS is a hyperelastic material with a linear stress-strain relationship up to 40% strain [35]. It is not clear if the strains were in the linear elastic regime in Greiner's and Kroner's works, and dissipation through fibrillar structures may be different from that in bulk materials [31].

Castellanos investigated the effect of separation rate on different epoxy adhesives patterned with 9-μm-diameter pillars with aspect ratio 1.1 and areal density 20%, using a 4-mm-diameter sapphire sphere and preload of 14 mN [13]. Adhesive force increased by an order-of-magnitude up to 6.8 mN over a range of damping factors from 0.5–0.8. Castellanos also reported a steeper increase in adhesive force with preload for adhesives with larger damping factors, which was attributed to a reduced ability to form rapid contact at high damping factors. The rate of indentation during preload was equal to the separation rate, meaning that contact area was also rate dependent. Rate dependent adhesion was only observed for low damping factor adhesives, indicating an equilibrium between increased energy dissipation and reduced contact area for

larger damping factors.

Areal density can make or break a fibrillar adhesive.

In a separate study by Aksak, PU adhesives with pillar heights from 30–100 μm, diameters from 4–25 μm, and inter-pillar spacing of 40 μm were investigated using a 12-mm-diameter glass sphere separated at 1 μm s^{-1} [3]. The adhesive force for PU patterned with 25-μm-diameter pillars was found to be 5 mN for aspect ratio 2.4 and 14 mN for aspect ratio three, significantly less than 18 mN for non-patterned samples. The areal density was 11.6% in both cases and a 30 mN preload was used (the adhesive force saturated for preloads above 5 mN). The authors found that non-patterned adhesives also exhibited preload dependence, concluding that viscous dissipation reduced the adhesive force for patterned adhesives. It is more likely that the areal density was too low for the chosen pillar radius.

The adhesion of polyimide (PI) pillars with diameters from 0.2–4 μm, heights from 0.15–2 μm, and pitches comparable to pillar diameter have been reported using a 50-μm-wide flat silicon AFM tip with a 10 mg preload [22]. The authors found that adhesive forces for all samples fell on a single curve, with adhesive force inversely proportional to the square of the array pitch. The authors conclude that adhesive force is directly proportional to areal density and only weakly dependent on pillar geometry. The authors have assumed that areal density is proportional to $\frac{1}{D^2}$; however it is actually proportional to $\frac{R}{D^2}$. This distinction is important as the radius is not constant in their work. Taking into account the varying pillar radius, there is a non-linear correlation between adhesive force and areal density. Significantly different adhesive forces were reported for different pillar radii at the same areal density, suggesting a significant dependence on pillar geometry.

Tsai *et al.* used flat silicon AFM tips to test the adhesion of square pillars in electron-beam lithography photoresist (ZEP 520A) with widths from 100–1900 nm, pitches from 200–2000 nm, and a height of 450 nm [74]. Adhesive strengths increased almost exponentially from 1–8 kPa with an increase in areal density from 15–90%.

Whilst we do not discuss hierarchically structured adhesives in this review, Glassmaker's work on film-terminated fibrillar adhesives gives an interesting insight into the effect of areal density

and contact area [23]. Glassmaker *et al.* studied the adhesion of PDMS films patterned with square pillars with width of 14 μm, heights from 50–60 μm, and pitches from 38–87 μm, capped with a 4–μm–thick PDMS film. A 3.97-mm-diameter glass sphere was separated at 1 μm s^{-1}. Increasing array pitch (thus decreasing areal density) was found to increase both the adhesive force and compliance. The adhesive force of non-patterned PDMS was reported to be 2.5 mN, whilst surface patterns with pitches of 38, 62 and 87 μm gave adhesive forces of 5, 8 and 11 mN, respectively. Evidently applying a continuous film reverses the dependence of adhesive force on areal density as the surface area is no longer dependent on areal density. The adhesive force ratio reported by Glassmaker is several times higher than that reported by Greiner [27] for comparable pillar size, areal density and substrate, owing to an increase in contact area.

Patterned adhesives are sensitive to substrate curvature and roughness.

A useful comparison between spherical and flat substrates can be found in Kroner's work, using PDMS adhesives with pillars of radius 4.7 μm, aspect ratios 0.2 and 0.4, and an areal density of 20% [39]. The adhesive forces for non-patterned PDMS and PDMS patterned with pillars of aspect ratio 0.2 and 0.4 were: 34, 12.5 and 15 mN, respectively, for a flat substrate; 1.9, 1.6 and 0.6 mN, respectively, for a 2-mm-diameter substrate, and; 5, 1 and 1.2 mN, respectively, for a 5-mm-diameter substrate. This comparison shows that adhesive force is highly dependent on substrate curvature, with patterned surfaces being more sensitive to curvature than non-patterned surfaces. The authors attribute this effect to misalignment between the spherical substrate and pillar tips at the edge of the contact region, consistent with measurements against the curved side of cylindrical probes [59], although misalignment effects are expected to be minimal with spherical substrates.

The effect of substrate roughness on the adhesion of silicon to PDMS pillars with diameters of 10 μm, aspect ratio two, and mushroom tips was investigated by Canas, using a separation rate of 5 μm s^{-1} [10]. The authors reported an almost exponential reduction in adhesive strength with increasing surface roughness, with adhesive strengths of 80 kPa and 5 kPa for root-mean-squared surface roughness of 2 nm and 618 nm, respectively. The authors concluded that

conformation and, hence, adhesion was influenced by the deepest topological features of the surface.

Adhesion to flat substrates is largely independent of preload.

Paretkar *et al.* investigated the adhesion of PDMS patterned with 10-μm-diameter pillars with aspect ratio three and areal density of 28%, using a 1-mm-diameter glass cylinder separated at 1 μm s^{-1} [54]. Non-patterned PDMS exhibited no preload dependence, with a constant adhesive strength of 8 kPa. In contrast, the adhesive strength for patterned PDMS was 30 kPa at zero preload and 60 kPa for all preloads up to 120 kPa. For preloads greater than 120 kPa pillars buckled and flipped into side contact, and the adhesive strength reduced to 1.2 kPa. Hence the relative adhesive strength was increased 3-fold with no preload and 7.5-fold following the application of a preload. In separate work, the authors reported a threshold preload value of 0.6 MPa, beyond which PDMS pillars of 10–20 μm diameter and 20 μm height began to buckle, with pillars eventually making side contact for preloads above 1.25 MPa [53].

Asymmetrical pillars exhibit directional adhesion.

An interesting study has been reported on the directional adhesion of half-cylinder PDMS fibrils (*i.e.* cylinders with a semi-circular cross-section) with radius of 5 μm, aspect ratio of four, and areal density of 15% [72]. The authors measured adhesion to a 4-mm-diameter glass puck for varying preloads, with and without shearing of the pillars prior to separation at 1 μm s^{-1}. The adhesive force without pre-shearing was 40 mN for the patterned adhesive, compared to 250 mN for flat PDMS at a preload of 100 mN. Interestingly, the adhesive force for the fibrillar adhesive could be increased or decreased by a factor of two by shearing in or against the direction of the flat pillar edge prior to separation, respectively. This arose from the difference in contact area between the top, flat edge and curved edge faces of the pillar. In a separate study the authors demonstrated significant preload dependence on adhesion after shearing towards the curved face [71]. Similarly, Parness *et al.* have shown that wedge-shaped pillars, with a wide base and narrow tip, exhibit negligible normal adhesion unless the pillars are pre-sheared to increase the contact area [55].

Adhesion to viscous films is improved with patterned adhesives

Patil investigated adhesion of PDMS patterned with square pillars with widths from 15–450 μm, pitch of twice the diameter, and height of 40 μm on a 10–μm–thick backing layer [56]. Instead of testing adhesion to a rigid substrate, a viscous PDMS (1% crosslinker by volume) film was cast directly over the adhesive and a flexible glass slide placed on the viscous film prior to peeling at 3 μm s^{-1}. The viscous liquid failed cohesively on non-patterned PDMS and adhesively on patterned PDMS, with an adhesive force with pillars twice the cohesive without pillars. The adhesive force was inversely proportional both to pillar width and array pitch.

Lower areal densities improve shear adhesion

Mahdavi *et al.* reported shear adhesion of poly(glycerol sebacate acrylate) (PGSA) adhesives patterned with conical structures with pillar diameters from 100 nm–1 μm and heights from 0.8–3 μm against porcine intestinal tissue [47]. The separation rate and preload were not disclosed. The adhesive force was inversely proportional both to the ratio of tip diameter to pitch, and the ratio of tip to base diameter. In other words, reducing either tip radius or areal density increased adhesion, and structures that are more resistant to shear deformation gave rise to larger adhesive forces. It is not clear from this study whether the pillars penetrated the skin akin to micro-needle arrays used for trans-dermal drug delivery [28, 30]. The pillars used in Mahdavi's work are of much lower heights than those typically used for micro-needle arrays, owing to the requirement to reach the dermis [30]. However, penetration of the epidermis could result in mechanical interlocking, rather than gecko-like adhesion.

Kramer *et al.* have investigated the shear adhesion of low-aspect-ratio PDMS hemispheres, with the flat surface presented for adhesion [38]. The authors measured shear adhesion to glass slides with zero preload, separated at 60 mm s^{-1}. The authors report adhesive strengths of 120$\pm$10 kPa for 50-μm-diameter pillars with areal density 20%, and 170$\pm$10 kPa, 160$\pm$5 kPa and 150$\pm$7 kPa for 100-μm-diameter pillars with areal densities of 10, 12, and 15%, respectively. These results suggest that adhesive force increases with increasing pitch, consistent with Mahdavi's work [47], and contrary to observations of peeling and normal separation.

Pillar angle gives direction-dependent adhesion

Jeong *et al.* investigated shear adhesion of polyurethane acrylate (PUA) adhesives patterned

with spatula-tipped pillars with diameters of 700 nm, 350 nm, and 600 nm at the bottom, neck, and tip respectively [32]. Backing layer thickness values of 50–60 μm were used, and shear adhesion was measured against the polished and rough faces of a silicon wafer, with a preload of 0.3 N cm^{-2}. The authors reported adhesive strengths against smooth Si of 30 kPa for smooth PUA and 150 kPa for PUA patterned with vertical pillars. For tilted pillars, the adhesive strength was 200 kPa and 2 kPa for pillars tilted at 30° towards and against the shear direction, respectively. For rough Si (rms=674 nm), the adhesive strength was negligible for non-pattered PUA and 55 kPa, 70 kPa and 15 kPa for vertical pillars and pillars tilted at 30° towards and against the shear direction, respectively. The adhesive strength against rough surfaces approximately halved owing to the size of the spatula precluding penetration of the topological features of the rough Si surface.

Similar direction-dependent adhesion has been reported for tilted PDMS pillars that were sheared in and against the tilt direction during preloading, followed by normal separation [14]. Boesel has also reported direction-dependent adhesion for tilted PUA pillars sheared under constant load [9], as has Kwak for triangular-tipped PDMS pillars peeled from a smooth glass surface [41]. Das *et al* investigated the effect of shear and tilt angle on contact area and found that contact area increased when sheared in the tilt direction and decreased when sheared against the tilt direction, and presented an analytical model of contact area consistent with JKR theory [18].

Mushroom-shaped pillars offer superior adhesion to flat punch

Del Campo *et al.* investigated the detachment load of pillars with different tip geometries using a 5–mm–diameter sapphire sphere separated normally from the array surface at 1 μm s^{-1} [19]. For pillars with aspect ratio of one, flat punch geometries enhanced adhesion only for a radius of 2.5 μm, larger radii resulted in reduced adhesion. Rounded punch and convex tip geometries both resulted in a loss of adhesion for pillar sizes from 2.5–25 μm. However, mushroom and spatula tip geometries were found to greatly enhance adhesion for pillar radii of 10 μm and 25 μm. The performance of spatula tip geometries lay between that of flat punch and mushroom geometries. The radius of the mushroom tip was not found to affect adhesion significantly, in

contrast to the underlying pillar radius. The findings of Del Campo are consistent with other reports of mushroom-tipped pillars [12, 16, 65, 69].

Mushroom-shaped PVS pillars have also been investigated for peel adhesion by Gorb *et al.* The patterned adhesive was peeled from a glass surface by fixing the load and varying the peeling angle to maintain a separation rate of 100 μm s^{-1}, after a preload of 50–130 mN [25]. The pillars had base and tip diameters of 60 μm and 25 μm, respectively, height of 100 μm, and a mushroom tip with diameter of 40 μm and thickness of 2 μm. The peeling strength for patterned adhesives was 40 N m^{-1}, compared to 22 N m^{-1} for non-patterned PVS. Gorb used Kendall's peeling model (Equation 8) to determine the fracture energy of the adhesive, which was found to be 1.38 and 0.51 J m^{-2} for the flat and patterned surfaces, respectively. The peeling force was independent of preload for both flat and patterned surfaces.

Mushroom-shaped pillars have also been tested against human skin [42]. PDMS (7.5% crosslinker) mushroom-tipped pillars with varying pillar and tip diameter, aspect ratio, and areal density were tested against the shaved skin on the back of a volunteer's hand under constant load following a preload of 0.3 N cm^{-2}. For 5-μm-diameter pillars with 9-μm-wide and 0.6-μm-thick mushroom cap with an areal density of 20%, the adhesive strength was comparable to non-patterned PDMS at 5 kPa for aspect ratios of one and two, but increased to 10 kPa and 9 kPa for aspect ratios of three and four, respectively.

The superiority of mushroom geometries is thought to arise from the concentration of stress within the contact area, as opposed to at the edges of the contact area for flat punch or convex tip geometries. In the latter, the stress concentration forces detachment to begin at the edges of the contact area, in contrast to mushroom geometries, in which detachment begins in the centre of the contact area [11, 12].

4 Concluding remarks

The major findings of this review can be summarised as follows:

- Small contact radius and large aspect ratios favour adhesion for normal, shear and peel

loading

- Larger adhesive forces are obtained at faster separation rates
- High areal densities are critical for normal and peel loading
- Low areal densities are favoured for shear loading
- Curvature and roughness of the substrate is critical
- Curved substrates give preload-dependent adhesion, flat substrates do not
- Asymmetrical or tilted fibres exhibit directional adhesion
- Fibrillar arrays improve adhesion to viscous films

The wide range of materials used for fibrillar adhesives gives rise to a range of Young's modulus from tens of kPa to several GPa, with varying degrees of viscoelasticity. For viscoelastic adhesives the adhesive force is rate-dependent, an effect investigated in only a few studies. The fact that adhesion is dependent on the material properties of the adhesive (in the limiting case of a rigid substrate the adhesive properties dominate) means that one cannot compare absolute adhesion between, for example, PDMS and PE. Instead, relative adhesive force and strength values are more useful measures to determine the efficacy of surface patterning; however, these can also be dependent on material properties if energy dissipation occurs in the fibrils.

The geometric parameters which influence the efficacy of patterned adhesives are fibre diameter, aspect ratio, areal density, and film thickness. We can relate the relationships between these parameters and adhesive strength to expectations of analytical models. Indeed, it is evident through numerous studies that decreasing pillar diameter and areal density increases adhesive strength under normal loading for both flat and spherical substrates, consistent with contact-splitting theory. However, if we take a step back from individual studies and compare relative adhesive forces across studies (see Figure 6) we see that, in Glassmaker's work [23], pillar radius and aspect ratio have little effect on relative adhesive force, whilst areal density has a profound effect. In Kroner [39] and Aksak's [3] works pillar radius and areal density have little effect, whereas aspect ratio does, and in Lee's work [46] areal density has little effect, whereas

pillar radius and aspect ratio do. Furthermore, we can estimate the relative adhesive force using JKR theory (see Appendix E), and we find the following dependencies on areal density, ρ, pillar radius, R, and circular geometric area of radius R_0 for several fibre geometries: (1) flat punch:

$$\frac{F_{patterned}}{F_{unpatterned}} = \rho^{1.25} R_0^{0.5} R^{-0.5}; \tag{25}$$

(2) curvature-invariant convex-ended pillars:

$$\frac{F_{patterned}}{F_{unpatterned}} = \rho^{1.5} R_0 R^{-1}; \tag{26}$$

and, (3) curvature-variant convex-ended pillars:

$$\frac{F_{patterned}}{F_{unpatterned}} = \rho^{2} R_0^{2} R^{-2} \ . \tag{27}$$

Unfortunately no single study investigates a sufficiently wide range of design parameters to verify these relationships. Geim *et al.* reported that adhesive force is directly proportional to the areal density using convex-ended pillars [22], Tsai *et al.* showed an almost exponential increase in adhesive strength with areal density for square posts [74], and Griener *et al.* reported a power law relationship between adhesive force and pillar radius with an exponent between -0.4 and -0.47 for flat-ended pillars [27]. None of these trends is accurately predicted by contact-splitting theory and the disparity becomes even more obvious when estimating the relative adhesive force for a given geometry. For an array of pillars with a radius of 1 μm, areal density of 20% and geometric radius of 1 cm, there are 2×10^7 pillars in the array. The predicted relative adhesive forces are 67, 4.5×10^3 and 2×10^7 for flat punch, self-similar scaling and curvature invariance, respectively, which are not consistent with reported data. Furthermore, the influence of aspect ratio is not fully considered in analytical models and individual pillars are unlikely to behave independently, a central assumption in the models reviewed here.

None of the analytical models discussed give insight into the effect of aspect ratio, despite a positive correlation between aspect ratio and adhesive strength under normal loading for both flat and spherical substrates. By considering the linear elastic deformation of a cylinder, it is trivial to show that the load required to impart unit strain energy is proportional to the square root of aspect ratio. Greiner *et al.* reported that adhesive strength exhibited a power law relationship with aspect ratio, with an exponent of 0.34. However, the fitted curve from which the exponent was calculated does not appear to be consistent with the data, and the goodness of fit is not discussed [27].

Surprisingly, areal density has the opposite effect on shear adhesion than that for normal and peel adhesion. We speculate that this correlation arises from an increasing contact area as pillars are sheared into side contact, which is reliant upon adequate separation between neighbouring pillars.

Several studies have shown a correlation between adhesive force and separation rate for viscoelastic materials, and there are examples of both positive and negative correlations between adhesion and separation rate for the same pillar geometry using different materials. This lack of consistency highlights the importance of material properties and the role of viscoelasticity in fibrillar adhesives, which is not yet fully understood.

In conclusion, it is apparent that reducing pillar diameter whilst increasing aspect ratio and areal density will increase adhesion for out-of-plane loading. In contrast, decreasing areal density is beneficial for in-plane loading. Although not an accurate model of fibrillar adhesion, the basic premise of contact-splitting theory — that adhesive strength can be enhanced through the use of smaller pillars — is supported by numerous studies.

Surprisingly, no study has yet identified a limit to the relative adhesion of fibrillar adhesives, although several authors have reported condensation or buckling of pillars at high aspect ratios. Pillar radius and aspect ratio are limited by the resolution of the fabrication process and material properties. The areal density can be increased until the gap between pillars is the limiting feature size and the adhesive is almost continuous. This poses an interesting question: how does adhesive strength behave as the gap between the pillars vanishes?

There are many interesting studies investigating asymmetrical or angled pillars, pillars with complex geometries, and hierarchical arrays of pillars-on-pillars, yet a multi-parametric study of simple flat-ended pillars for a meaningful range of pillar geometries, materials, and loading conditions is lacking. Such a study would be beneficial to understand how geometric parameters influence adhesion, allowing fibrillar adhesives to be optimised for specific applications.

Table 4 near here.

Table 5 near here.

Table 1: Table of symbols. Dashes indicate dimensionless parameters.

Symbol	Description	Units
δ	Displacement	m
F	Adhesive force	N
G	Adhesive strength	N m^{-2}
R	Pillar or sphere radius	m
h	Fibril height	m
α	Fibril aspect ratio	–
ρ	Areal density of fibrils	–
A	Geometric area of adhesive	m^2
n	Number of fibrils in array	–
σ	Stress	N m^{-2}
D	Array pitch	m
W	Work of adhesion	J m^{-2}
E	Young's modulus	N m^{-2}
ν	Poisson ratio	–
μ	Shear modulus	N m^{-2}
γ	Surface energy	J m^{-2}
z_0	Equilibrium spacing in Lennard-Jones potential	m
t	Film thickness	m
b	Film width	m
θ	Peeling angle from surface	deg
c	Peeling distance	m
P	Preload force	N
a	Contact radius	m
k	Spring constant	N m^1
U_E	Elastic energy	J
U_P	Potential energy	J
U_S	Surface energy	J

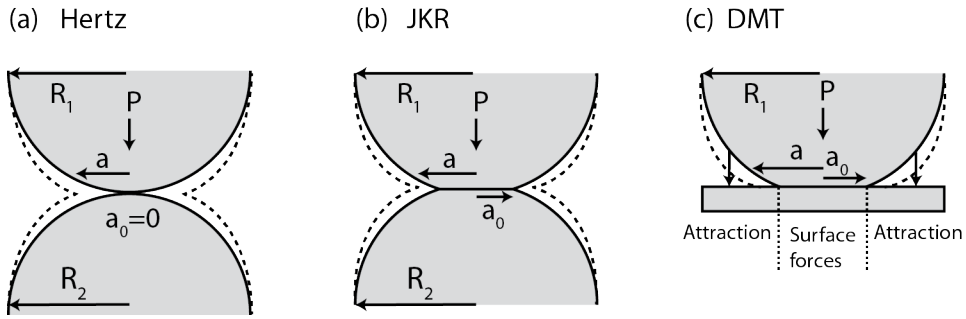

Figure 1: Cross-sectional illustration of the contact between two elastic spheres for (a) Hertz contact, (b) JKR, and (c) DMT models. No interactions are considered in Hertz theory, only surface forces within the contact region are considered in JKR theory, and both surface forces within and attractive forces without the contact region are considered in DMT theory. Solid lines indicate contact configuration at zero load and dashed lines indicate contact configuration for an applied load, P. (a) and (b) redrawn from [33].

Table 2: Key relationships from Hertz, JKR and DMT theories

Author	Compressive load displacement relationship	Contact radius at zero load	Adhesive force
Hertz [33]	$\delta = \frac{2}{3}\frac{P}{Ka}$	$a_0 = 0$	$F = 0$
JKR [33]		$a_0 = \left(\frac{6\pi\gamma R^{*2}}{K}\right)^{\frac{1}{3}}$	$F = \frac{3}{2}\pi\gamma R^*$
DMT [20, 48, 49]		$a_0 = \left(\frac{4\pi\gamma R^{*2}}{K}\right)^{\frac{1}{3}}$	$F = 2\pi\gamma R^*$

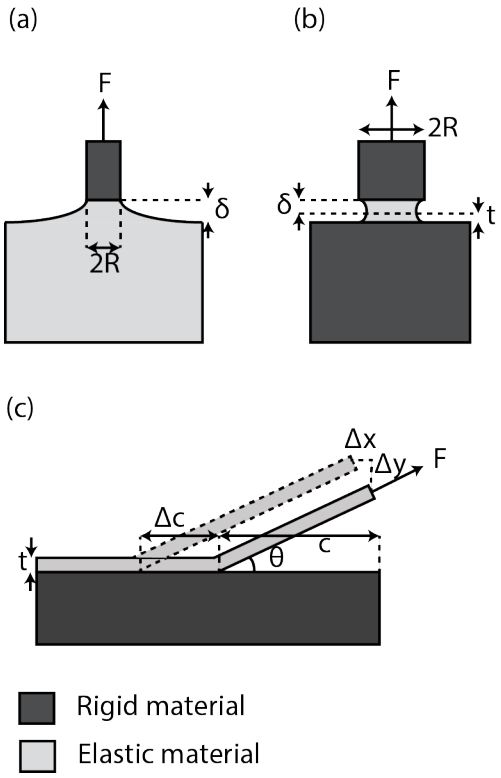

Figure 2: Illustration of the normal separation of (a) a rigid cylinder from an elastic half-space and (b) a thin elastic film between a rigid cylinder and a rigid half-space and (c) an elastic film peeled from a rigid substrate. The un-deformed film thickness is given by t. Redrawn, with additions, from [36].

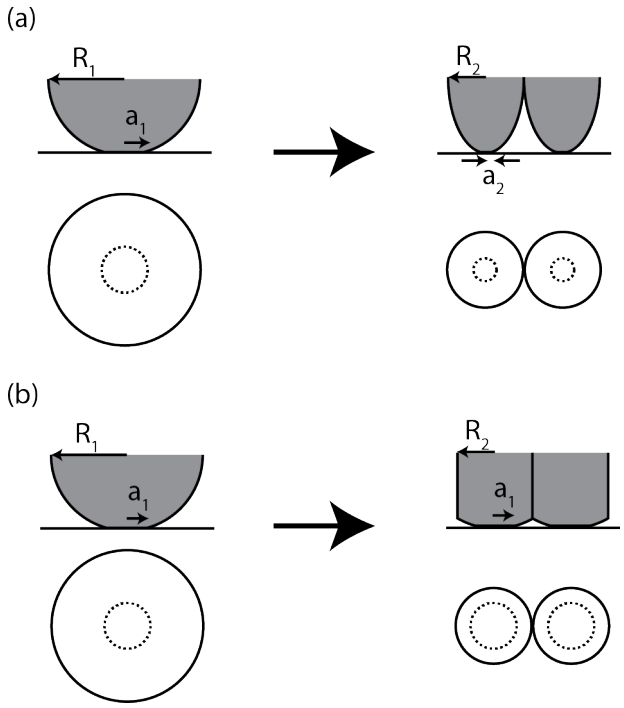

Figure 3: Illustration of the contact-splitting principle for (a) self-similar scaling and (b) curvature invariance. Top-down and side-on views are shown. Dotted lines illustrate actual contact area in top-down view. For self-similar scaling the contact area scales with $n^{\frac{2}{3}}$ and the adhesive force scales with $n^{0.5}$. For curvature invariance the contact area and adhesive force both scale with n. A value of $n = 2$ has been used for illustrative purposes.

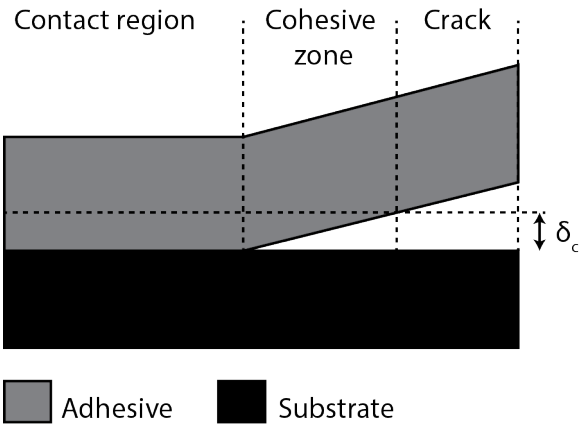

Figure 4: Illustration of the cohesive zone, a region outside the contact region where the interface is separated by less than a critical distance, δ_c, and is still held by adhesive forces. For separations greater than δ_c, adhesive forces no longer exist and a crack opens.

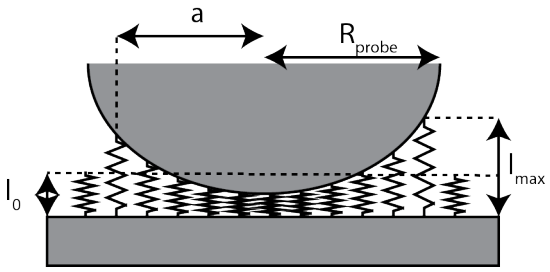

Figure 5: Illustration of the contact between a sphere and a pillar array at equilibrium (i.e. zero load) using spring contact theory - redrawn from [66]

.

Table 3: Summary of major findings

1	Small contact radius and large aspect ratios favour adhesion for normal, shear and peel loading
2	Larger adhesive forces are obtained at faster separation rates
3	High areal densities are critical for normal and peel loading
4	Low area densities are favoured for shear loading
5	Curvature and roughness of the substrate is critical
6	Curved substrates give preload-dependent adhesion, flat substrates don't
7	Asymmetrical or tilted fibres exhibit directional adhesion
8	Fibrillar arrays improve adhesion to viscous films

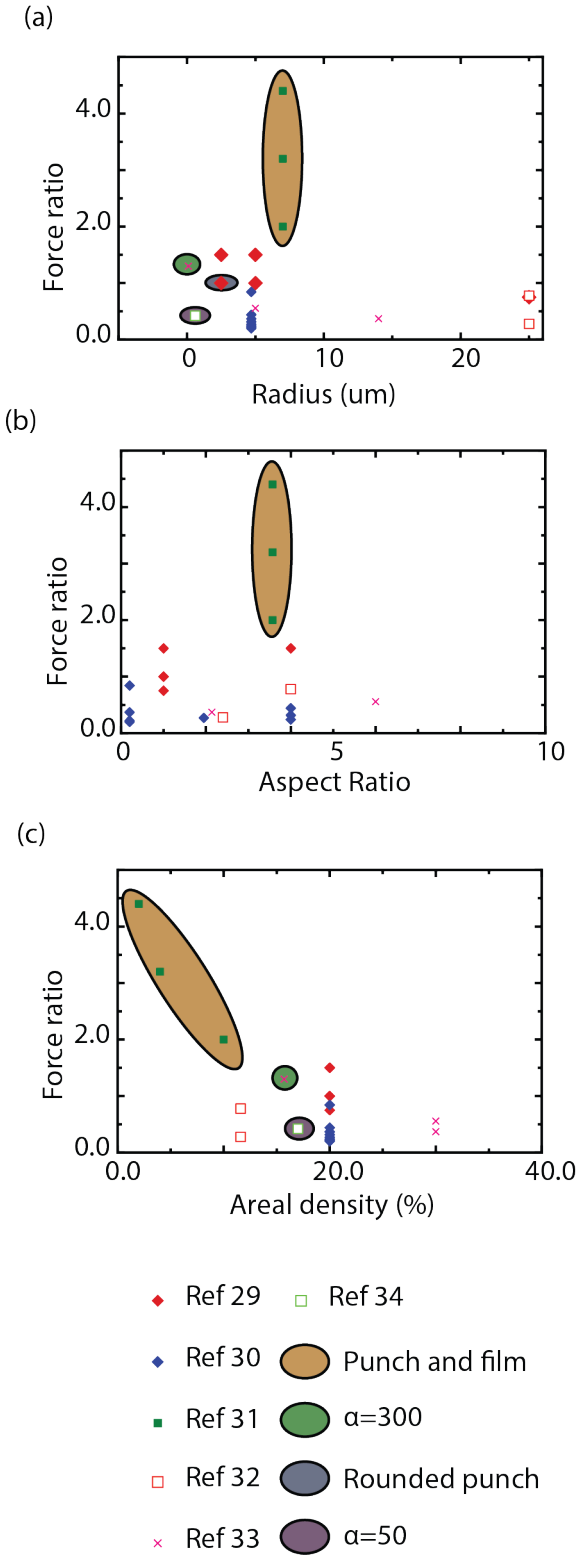

Figure 6: Plots of adhesive force ratio (ratio of adhesive forces for patterned and flat surfaces) under normal loading as a function of (a) fibre radius, (b) aspect ratio and (c) areal density. Values have been taken from Table 4; references are given in the figure legend. Special attention has been drawn to specific data which have unusual properties, such as large aspect ratio and non-standard fibre geometry, where those data points are identifiable.

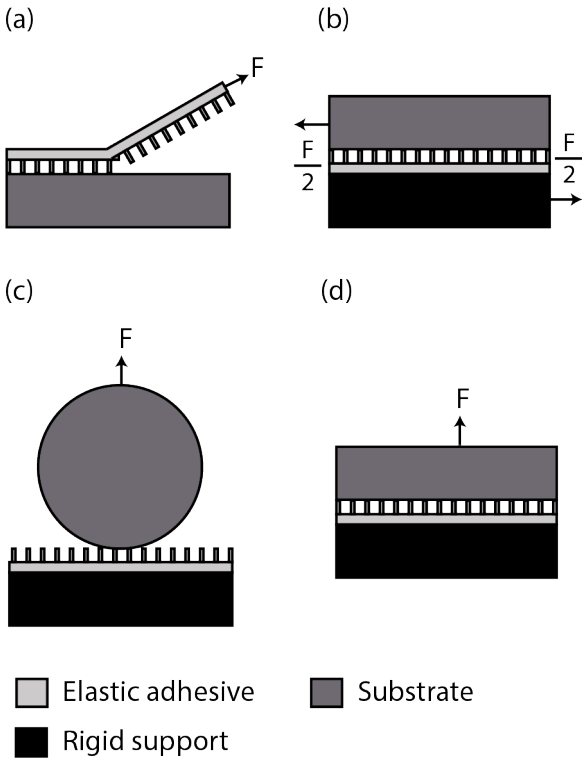

Figure 7: Illustration of different loading configurations for adhesive measurements - (a) peel adhesion, (b) tensile (or shear) adhesion, and normal adhesion using (c) a spherical probe and (d) and a flat probe.

Table 4: Summary of fibrillar adhesive performance under normal loading. For curved substrates, the diameter is given by ϕ.R is the fibre radius, α is the aspect ratio, ρ is the areal density, ϕ is the spherical substrate diameter, F is the adhesive force and G is the adhesive strength.

Material	Type	R μm	α	ρ %	Preload	Rate	ϕ (μm s^{-1})	F	G	Adhesive force ratio	Adhesive strength ratio	Ref.
PDMS	Punch	2.5	1	20	4 mN	1	5 mm	1.2 mN	18 kPa	1.50	—	[27]
PDMS	Punch	5	1	20	4 mN	1	5 mm	0.8 mN	12 kPa	1.00	—	[27]
PDMS	Punch	25	1	20	4 mN	1	5 mm	0.6 mN	9 kPa	0.750	—	[27]
PDMS	Punch	5	4	20	4 mN	1	5 mm	1.3 mN	19.5 kPa	1.50	—	[27]
PDMS	Rounded punch	2.5	1	20	4 mN	1	5 mm	0.8 mN		1.00	—	[27]
PDMS	Mushroom	25	4	20	10 mN	1	5 mm	5 mN	—	—	—	[27]
PDMS	Spatula	25	4	20	10 mN	1	5 mm	3 mN	—	—	—	[27]
PDMS	Punch	4.7	0.2	20	2 mN	5	5 mm	1 mN	—	0.220	—	[39]
PDMS	Punch	4.7	1.95	20	2 mN	5	5 mm	1.2 mN	—	0.270	—	[39]
PDMS	Punch+ film	7	3.57	10	—	1	3.97 mm	5 mN	—	2.00	—	[23]
PDMS	Punch+ film	7	3.57	4	—	1	3.97 mm	8 mN	—	3.20	—	[23]
PDMS	Punch+ film	7	3.57	2	—	1	3.97 mm	11 mN	—	4.40	—	[23]
PU	Punch	25	2.4	11.6	30 mN	1	12 mm	5 mN	—	0.278	—	[3]
PU	Punch	25	4	11.6	30 mN	1	12 mm	14 mN	—	0.778	—	[3]
PP	Punch	0.1	300	15.7	—	—	30 μm	350 nN	—	1.30	—	[46]
PP	Punch	5	6	30	—	—	30 μm	150 nN	—	0.556	—	[46]
PP	Punch	14	2.14	30	—	—	30 μm	100 nN	—	0.370	—	[46]
PP	Punch	0.6	50	17	—	—	30 μm	180$\pm$100 nN	—	0.421–2.55	—	[52]
PDMS	Punch	4.7	0.2	20	—	—	5 mm	1 mN	—	0.200	—	[39]
PDMS	Punch	4.7	4	20	—	—	5 mm	1.2 mN	—	0.240	—	[39]
PDMS	Punch	4.7	0.2	20	—	—	2 mm	1.6 mN	—	0.842	—	[39]
PDMS	Punch	4.7	4	20	—	—	2 mm	0.6 mN	—	0.316	—	[39]
PDMS	Punch	4.7	0.2	20	—	—	Flat	12.5 mN	—	0.368	—	[39]
PDMS	Punch	4.7	4	20	—	—	Flat	15 mN	—	0.441	—	[39]
PDMS	Punch	5	3	28	0	1	Flat	—	30 kPa	—	3.75	[54]
PDMS	Punch	5	3	28	120 kPa	1	Flat	—	60 kPa	—	7.50	[54]
ZEP 520A	Punch	0.05	4.5	15	—	—	Flat	—	1 kPa	—	—	[74]
ZEP 520A	Punch	1.9	4.5	90	—	—	Flat	—	8 kPa	—	—	[74]
PDMS	Half-punch	5	4	15	100 mN	1	Flat	40 mN	—	0.16	—	[72]
PDMS	Punch	5	2	—	—	5	Si (rms=2 nm)	—	80 kPa	—	—	[10]
PDMS	Punch	5	2	—	—	5	Si (rms=618 nm)	—	5 kPa	—	—	[10]

References

[1] AHMADI, S., AND MENON, C. A new model for predicting fibre clumping phenomenon in bio-inspired dry adhesives. *The Journal of Adhesion 90* (2014), 135–155.

[2] AKSAK, B., HUI, C., AND SITTI, M. The effect of aspect ratio on adhesion and stiffness for soft elastic fibres. *Interface 8* (2011), 1166–1175.

[3] AKSAK, B., MURPHY, B., AND SITTI, M. Adhesion of biologically inspired vertical and angled polymer microfiber arrays. *Langmuir 23*, 6 (2007), 3322–32.

[4] ALFANO, M., FURGIUELE, F., LEONARDI, A., MALETTA, C., AND PAULINO, G. Cohesive zone modelling of mode 1 fracture in adhesive bonded joints. *Key Engineering Materials 348-349* (2007), 13–16.

[5] ARZT, E., GORB, S., AND SPOLENAK, R. From micro to nano contacts in biological attachment devices. *Proceedings of the National Academy of Sciences of the United States of America 100*, 19 (2003), 10603–6.

[6] AUTUMN, K., HSIEH, S., DUDEK, D., CHEN, J., CHITAPHAN, C., AND FULL, R. Dynamics of geckos running vertically. *The Journal of Experimental Biology 209* (2005), 260–272.

[7] BARENBLATT, G. Mathematical theory of equilibrium cracks in brittle features. *Advanced Applied Mechanics 7* (1962), 55–129.

[8] BHUSHAN, B., AND SAYER, R. *Nanotribology and Nanomechanics*. 2011.

[9] BOESEL, L., GREINER, C., ARZT, E., AND DEL CAMPO, A. Gecko-inspired surfaces: a path to strong and reversible dry adhesives. *Advanced Materials 22*, 19 (2010), 2125–37.

[10] CANAS, N., KAMPERMAN, M., VOLKER, B., KRONER, E., AND MCMEEKING, R. M. Effect of nano and micro roughness on adhesion of bioinspired micropatterned surfaces. *Acta Biomaterialia 8* (2012), 282–288.

[11] CARBONE, G., AND PIERRO, E. Sticky bio-inspired micropillars: finding the best shape. *Small 8* (2012).

Table 5: Summary of fibrillar adhesive performance under shearing (S) and peeling (P). R is the fibre radius, α is the aspect ratio, ρ is the areal density, ϕ is the spherical substrate diameter, F is the adhesive force, G is the adhesive strength. PIT refers to porcine intestinal tissue and skin refers to human skin (the back of a hand).

Material	Type	R μm	α	ρ %	Preload	Rate (μm s^{-1})	Mode	Substrate	F	G	Adhesive force ratio	Adhesive strength ratio	Ref.
PDMS	Punch	1	0.35	17	50 kPa	6	P	Glass	120 mN	—	2.00	—	[45]
PDMS	Square post	15	2.67	—	—	3	P	PDMS	450 mN	—	2	—	[56]
PDMS	Mushroom	5, 9	1	20	0.3 Pa	—	P	Skin	—	5 kPa	—	1	[41]
PDMS	Mushroom	5, 9	3	20	0.3 Pa	—	P	Skin	—	10 kPa	—	2	[41]
PVS	Mushroom	25, 40	4	—	130 mN	—	P	Glass	40 N m^{-1}	—	1.82	—	[25]
PGSA	Punch	0.18	—	0.34	—	—	S	PIT	—	—	—	2.5	[47]
PGSA	Punch	0.4	—	2.85	—	—	S	PIT	—	—	—	2	[47]
PGSA	Punch	0.4	—	16.6	—	—	S	PIT	—	—	—	1.2	[47]
PUA	Spatula	0.7, 0.35, 600	—	—	3 kPa	—	P	Flat Si	—	150 kPa	—	5	[32]
PDMS	Hemishpere	25	—	10	—	60 10^3	S	Glass	—	120 kPa	—	—	[38]
PDMS	Hemishpere	50	—	10	—	60 10^3	S	Glass	—	170 kPa	—	—	[38]
PDMS	Hemishpere	50	—	12	—	60 10^3	S	Glass	—	160 kPa	—	—	[38]
PDMS	Hemishpere	50	—	15	—	60 10^3	S	Glass	—	150 kPa	—	—	[38]

[12] CARBONE, G., PIERRO, E., AND GORB, S. Origin of the superior adhesive performance of mushroom-shaped microstructure surfaces. *Soft Matter 7* (2011), 5545–5552.

[13] CASTELLANOS, G., ARZT, E., AND KAMPERMAN, M. Effect of viscoelasticity on adhesion of bioinspired micropatterned epoxy surfaces. *Langmuir 27*, 12 (2011), 7752–9.

[14] CHARY, S., TAMELIER, J., AND TURNER, K. L. A microfabricated gecko-inspired controllable and reusable dry adhesive. *Smart Materials and Structures 22* (2012).

[15] CHEN, H., FENG, X., AND CHEN, Y. Directionally controlled transfer printing using micropatterned stamps. *Applied Physics Letters 103* (2013).

[16] CHEUNG, E., AND SITTI, M. Adhesion of biologically inspired polymer microfibres on soft surfaces. *Langmuir 25* (2009), 6613–6616.

[17] DAI, Z., YU, M., AND GORB, S. Adhesion characteristics of polyurethane for bionic hairy foot. *Journal of Intelligent Material Systems and Structures 17* (2006), 737–741.

[18] DAS, S., CHARY, S., YU, J., TAMELIER, J., TURNER, K., AND ISRAELACHVILI, J. Jkr theory for the stick-slip peeling and adhesion hysteresis of gecko mimetic patterned surfaces with a smooth glass surface. *Langmuir 29* (2013), 15006–15012.

[19] DEL CAMPO, A., GREINER, C., AND ARZT, E. Contact shape controls adhesion of bioinspired fibrillar surfaces. *Langmuir 23*, 20 (2007), 10235–43.

[20] DERJAGUIN, B., MULLER, V., AND TOPOROV, Y. Effect of contact deformations on the adhesion of particles. *Journal of Colloid and Interface Science 53*, 2 (1975).

[21] DUGDAL, D. Yielding of steel sheets containing slits. *Journal of the Mechanics and Physics of Solids 8* (1960), 100–104.

[22] GEIM, A., DUBONOS, S., GRIGORIEVA, I., NOVOSELOV, K., ZHUKOV, A., AND SHAPOVAL, S. Microfabricated adhesive mimicking gecko foot-hair. *Nature materials 2*, 7 (2003), 461–3.

[23] GLASSMAKER, N., AND JAGOTA, A. Biologically inspired crack trapping for enhanced adhesion. *PNAS 104*, 26 (2007), 1–6.

[24] GORB, S. J., JIAO, Y., AND SCHERGE, M. Ultrastructural architecture and mechanical properties of attachment pads in tettigonia viridissima. *Journal of Computational Physiology 186* (2000), 821–831.

[25] GORB, S. N., AND VARENBERG, M. Mushroom-shaped geometry of contact elements in biological adhesive systems. *Journal of Adhesion Science and Technology 21*, 12-13 (2007), 1175–1183.

[26] GREINER, C., BUHL, S., DEL CAMPO, A., AND ARZT, E. Experimental parameters controlling adhesion of biomimetic fibrillar surfaces. *The Journal of Adhesion 85* (2009), 646–661.

[27] GREINER, C., CAMPO, A. D., AND ARZT, E. Adhesion of bioinspired micropatterned surfaces: effects of pillar radius, aspect ratio, and preload. *Langmuir 23*, 7 (2007), 3495–502.

[28] HENRY, S., MCALLISTER, D., ALLEN, M., AND PRAUSNITZ, M. Microfabricated microneedles: a novel approach to transdermal drug delivery. *Journal of pharmaceutical sciences 87* (1998), 922–925.

[29] HUI, C.-Y., AND JAGOTA, A. Constraints on microcontact printing imposed by stamp deformation. *Langmuir 18* (2002), 1394–1407.

[30] INDERMUN, S., LUTTGE, R., CHOONARA, Y., KUMAR, P., DU TOIT, L., MODI, G., AND PILLAY, V. Current advances in the fabrication of microneedles for transdermal drug delivery. *Journal of Controlled Release 185* (2014), 130–138.

[31] JAGOTA, A., AND BENNISON, S. J. Mechanics of adhesion through a fibrillar microstructure. *Integrative and comparative biology 42*, 6 (2002), 1140–5.

[32] JEONG, H., LEE, J., KIM, H., MOON, S. H., AND SUH, K. Y. A nontransfering dry adhesive with hierarchical polymer nanohairs. *Proceedings of the National Academy of Sciences of the United States of America 106*, 4 (2009), 5639–5644.

[33] JOHNSON, K. Surface energy and the contact of elastic solids. *Proceedings of the Royal Society A 324* (1971), 301–313.

[34] JOHNSON, K., AND GREENWOOD, J. An adhesion map for the contact of elastic spheres. *Journal of Colloid and Interface Science 192* (1997), 326–333.

[35] JOHNSTON, I., MCCLUSKEY, D., TAN, C., AND TRACEY, M. Mechanical characterisation of bulk sylgard 184 for microfluidics and microengineering. *Journal of Micromechanics and Microengineering 24* (2014).

[36] KENDALL, K. The adhesion and surface energy of elastic solids. *Journal of Physics D: Applied Physics 4* (1971), 1186–1195.

[37] KENDALL, K. Thin-film peeling-the elastic term. *Journal of Physics D: Applied Physics 8* (1975), 1449–1452.

[38] KRAMER, R., MAJIDI, C., AND WOOD, R. Shear-mode contact splitting for a microtextured elastomer film. *Advanced Materials 22* (2010), 3700–3703.

[39] KRONER, E., PARETKAR, D., MCMEEKING, R., AND ARZT, E. Adhesion of flat and structured pdms samples to spherical and flat probes: A comparative study. *The Journal of Adhesion 87*, 5 (2011), 447–465.

[40] KWAK, J., AND KIM, T. A review of adhesion and friction models for gecko feet. *International Journal of Precision Engineering and Manufacturing 11* (2010), 171–186.

[41] KWAK, M., JEONG, H., BAE, W., JUNG, H., AND SUH, K. Y. Anisotropic adhesion properties of triangular-tip-shaped micropillars. *Small 7*, 16 (2011), 2296–2300.

[42] KWAK, M., JEONG, H., AND SUH, K. Y. Rational design and enhanced biocompatability of a dry adhesive medical skin patch. *Advanced Materials 23* (2011), 3949–3953.

[43] LAKE, G. Fatigue and fracture of elastomers. *Rubber Chemistry and Technology 68* (1995), 435–460.

[44] LAKE, G., AND THOMAS, A. The strength of highly elastic materials. *Proceedings of the Royal Society A 300* (1967), 108–119.

[45] LAMBLET, M., VERNEUIL, E., VILMIN, T., BUGUIN, A., SILBERZAN, P., AND LÉGER, L. Adhesion enhancement through micropatterning at polydimethylsiloxane-acrylic adhesive interfaces. *Langmuir 23*, 13 (2007), 6966–74.

[46] LEE, H., AND BUSHAN, B. Fabrication and characterisation of hierarchical nanostructured smart adhesion surfaces. *Journal of Colloid and Interface Science 372* (2012), 231–238.

[47] MAHDAVI, A., FERREIRA, L., SUNDBACK, C., NICHOL, J., CHAN, E., CARTER, D. J., BETTINGER, C., PATANAVANICH, S., CHIGNOZHA, L., BEN-JOSEPH, E., GALAKATOS, A., PRYOR, H., POMERANTSEVA, I., MASIAKOS, P., FAQUIN, W., ZUMBUEHL, A., HONG, S., BORENSTEIN, J., VACANTI, J., LANGER, R., AND KARP, J. A biodegradable and biocompatible gecko-inspired tissue adhesive. *Proceedings of the National Academy of Sciences of the United States of America 105*, 7 (2008), 2307–12.

[48] MAUGIS, D. Adhesion of spheres: the jkr-dmt transition using a dugdale model. *Journal of Colloid and Interface Science 150*, 1 (1992).

[49] MULLER, V., DERJAGUIN, B., AND TOPOROV, Y. On two methods of calculation of the force of sticking of an elastic sphere to a rigid plane. *Colloids and Surfaces 7* (1983), 251.

[50] MULLER, V., YUSHENKO, V., AND DERJAGUIN, B. On the influence of molecular forces on the deformation of an elastic sphere and its sticking to a rigid plane. *Journal of Colloid and Interface Science 77*, 91 (1980).

[51] NADERMANN, N., KUMAR, A., GOYAL, S., AND HUI, C. Buckling of sheared and compressed microfibrils. *Interface 7* (2010), 1581–1589.

[52] PALACIO, M., BUSHAN, B., AND SCHRICKER, S. Gecko-inspired fibril nanostrcutres for reversible adhesion in biomedical applications. *Materials Letters 92* (2013), 409–412.

[53] PARETKAR, D., BARTLETT, M., MCMEEKING, R., CROSBY, A., AND ARZT, E. Buckling of an adhesive polymeric micropillar. *The Journal of Adhesion 89* (2013), 140–158.

730 [54] PARETKAR, D., KAMPERMAN, M., SCHNEIDER, A., MARTINA, D., CRETON, C.,
731 AND ARZT, E. Bioinspired pressure actuated adhesive system. *Materials Science and*
732 *Engineering: C 31*, 6 (2011), 1152–1159.

733 [55] PARNESS, A., SOTO, D., ESPARZA, N., GRAVISH, N., WILKINSON, M., AUTUMN,
734 K., AND CUTKOSKY, M. A microfabricated wedge-shaped adhesive array displaying
735 gecko-like dynamic adhesion, directionality and long lifetime. *Interface 6* (2009), 1223–
736 1232.

737 [56] PATIL, S., MANGAL, R., MALASI, A., AND SHARMA, A. Biomimetic wet adhesion
738 of viscoelastic liquid films anchored on micropatterned elastic substrates. *Langmuir 28*
739 (2012), 14784–14791.

740 [57] PEATTIE, A., AND FULL, R. J. Phylogenetic analysis of the scaling of wet and dry
741 biological fibrillar adhesives. *Proceedings of the National Academy of Sciences of the*
742 *United States of America 104*, 47 (2007), 18595–18600.

743 [58] PEATTIE, A., MAJIDI, C., CORDER, A., AND FULL, R. J. Ancestrally high elastic
744 modulus of gecko setal beta-keratin. *Journal of the Royal Society Interface 4*, 17 (2007),
745 1071–1076.

746 [59] PERESSADKO, A., AND GORB, S. When less is more: Experimental evidence for tenac-
747 ity enhancement by division of contact area. *The Journal of Adhesion 80*, 4 (2004),
748 247–261.

749 [60] PERSSON, B. N. J. On the mechanism of adhesion in biological systems. *The Journal of*
750 *Chemical Physics 118*, 16 (2003), 7614.

751 [61] PERSSON, B. N. J. Biological adhesion for locomotion: basic principles. *Journal of*
752 *Adhesion Science and Technology 21*, 12-13 (2007), 1145–1173.

753 [62] PESIKA, N., TIAN, Y., ZHAO, B., ROSENBERG, K., ZENG, H., MCGUIGGAN, P.,
754 AUTUMN, K., AND ISRAELACHVILI, J. Peel-zone model of tape peeling based on the
755 gecko adhesive system. *The Journal of Adhesion 83* (2007), 383–401.

[63] RODRÍGUEZ, I., LIM, C., NATARAJAN, S., HO, A., VAN, E. L., ELMOUELHI, N., LOW, H., VYAKARNAM, M., AND COOPER, K. Shear adhesion strength of gecko-inspired tapes on surfaces with variable roughness. *The Journal of Adhesion 89* (2013), 921–936.

[64] SAMEOTO, D., AND MENON, C. Recent advances in the fabrication and adhesion testing of biomimetic dry adhesives. *Smart Materials and Structures 19* (2010).

[65] SAMEOTO, D., SHARIF, H., TELLEZ, J., FERGUSON, B., AND MENON, C. Nonangles anisotopic elastomeric dry adhesives with tailorable normal adhesion strength and high directionality. *Journal of Adhesion Science and Technology 28*, 3-4 (2014), 354–366.

[66] SCHARGOTT, M., POPOV, V. L., AND GORB, S. Spring model of biological attachment pads. *Journal of theoretical biology 243*, 1 (2006), 48–53.

[67] SHI, X., AND ZHAO, Y. Comparison of various adhesion contact theories and the influence of dimensionless load parameter. *Journal of Adhesion Science and Technology 18*, 1 (2004), 55–68.

[68] SPOLENAK, R., GORB, S., GAO, H., AND ARZT, E. Effects of contact shape on the scaling of biological attachments. *Proceedings of the Royal Society A: Mathematical, Physical and Engineering Sciences 461*, 2054 (2005), 305–319.

[69] SPUSKANYUK, A., MCMEEKING, R., DESHPANDE, V., AND ARZT, E. The effect of shape on the adhesion of fibrillar surfaces. *Acta Biomaterialia 4*, 6 (2008), 1669–76.

[70] TABOR, D. Surface forces and surface interactions. *Journal of Colloid and Interface Science 58*, 1 (1977).

[71] TAMELIER, J., CHARY, S., AND TURNER, K. Importance of loading and unloading procedures for gecko-inspired controllable adhesives. *Langmuir 29* (2013), 10881–10890.

[72] TAMELIER, J., CHARY, S., AND TURNER, K. L. Vertical anisotropic microfibres for a gecko inspired adhesive. *Langmuir 28* (2012), 8746–8752.

[73] TANG, T., HUI, C.-Y., AND GLASSMAKER, N. Can a fibrillar interface be stronger and tougher than a non-fibrillar one? *Journal of the Royal Society Interface 2* (2005), 505–516.

[74] TSAI, Y., WU, M., AND SHIH, W. Fabrication and characterisation of e-beam photoresist array for biomimetic self-cleaning dry adhesives. *Microelectronic Engineering 88* (2011), 2126–2128.

[75] VARENBERG, M., MURARASH, B., KLIGERMAN, Y., AND GORB, S. Geometry controlled adhesion: revisiting the contact splitting hypothesis. *Applied Physics A 103* (2011).

[76] YANG, F., AND LI, J. Adhesion of a rigid punch to an incompressible elastic film. *Langmuir 17* (2001), 6524–6529.

[77] YU, J., AND BULOVIC, V. Micropatterning metal electrode of organic light emitting devices using rapid pdms lift-off. *Applied Physics Letters 91* (2007).

[78] ZALKOVSKIJ, M., THAMDRUP, L., SMISTRUP, K., ANDEN, T., JOHANSSON, A., MIKKELSEN, N., MADSEN, M., GARNAES, J., KRISTIANSEN, T., DIEMER, M., DOSSING, M., MINZARI, D., TANG, P., KRISTENSEN, A., TABORYSKI, R., ESSENDROP, S., NIELSEN, T., AND BILENBERG, B. Smart plastic functionalization by nanoimprint and injection molding. *Proc. SPIE 9423 Alternative Lithographic Technologies VII* (2015).

[79] ZHOU, M., PESIKA, N., ZENG, H., TIAN, Y., AND ISRAELACHVILI, J. Recent advances in gecko adhesion and friction mechanisms and development of gecko-inspired dry adhesive systems. *Friction 1* (2013), 114–129.

[80] ZHOU, M., PESIKA, N., ZENG, H., WAN, J., ZHANG, X., MENG, Y., WEN, S., AND TIAN, Y. Design of gecko-inspired fibrillar surfaces with strong attachment and easy-removal properties: a numerical analysis of peel-zone. *Interface 9* (2012), 2424–2436.

[81] ZHOU, M., TIAN, Y., PESIKA, N., ZENG, H., WAN, J., MENG, Y., AND WEN, S. The extended peel zone model: effect of peeling velocity. *The Journal of Adhesion 87* (2011), 1045–1058.

5 Appendix A

Rigid cylinder in contact with an elastic half-space

In the case of a flat -ended, rigid cylinder in contact with an elastic half-space (Figure 2 (b)), the deformation, δ, of the elastic half-space when a force, F, is applied to the cylinder is given by [36]:

$$\delta = \frac{F\left(1-\nu^2\right)}{2ER} \ . \tag{28}$$

The stored elastic energy, U_E, is found by rearranging Equation 28 and integrating the force, F, with respect to deformation, δ, giving:

$$U_E = \frac{F^2\left(1-\nu^2\right)}{4ER} + C_E \ , \tag{29}$$

where C_E is a constant of integration. The surface energy, U_S, is the product of surface energy per unit area, γ, and the area of contact. The potential energy of the load, U_P, is the product of the force and displacement. The surface and potential energies are given by:

$$U_S = -\pi R^2 \gamma \ , \tag{30}$$

$$U_P = -\frac{F^2\left(1-\nu^2\right)}{2ER} + C_P \ , \tag{31}$$

where C_P is a constant of integration. The total energy, U_T, is the sum of the surface energy, U_S, and the potential energy of the load, U_P, given by:

$$U_T = -\pi R^2\gamma + \frac{\left(1-\nu^2\right)F^2}{4ER} - \frac{\left(1-\nu^2\right)F^2}{2ER} + C_E + C_P = 0 \ . \tag{32}$$

Equilibrium peeling occurs when the differential of total energy across the contacting surfaces

(with respect to R) is zero, i.e.

$$\frac{dU_T}{dR} = 0 \ . \tag{33}$$

Differentiating Equation 32 according to Equation 33 gives

$$-2\pi R\gamma + \frac{(1-\nu^2)\,F^2}{4ER^2} = 0 \ . \tag{34}$$

The adhesive force, F, can be found by rearranging Equation 34 to give Equation 6, which is repeated below:

$$F = \sqrt{\frac{E}{(1-\nu^2)} 8\pi\gamma R^3} \ ,$$

Equation 6 was shown by Kendal to accurately fit experimental data for the separation of acrylic disks from gelatin sheets for disk diameters ranging from 1–4 cm [36].

6 Appendix B

Thin elastic layer between a rigid cylinder and rigid half-space

For an elastic layer of thickness t between a rigid cylinder of radius R and a rigid surface, the total energy, U_T, is given by [36]:

$$U_T = -\pi R^2\gamma - \frac{F^2 t}{2\pi R^2}\frac{3\,(1-2\nu)}{E} \ . \tag{35}$$

Applying Equation 33, we get an adhesive force, F, given by Equation 7, repeated below:

$$F = \sqrt{\frac{2\pi^2\gamma R^4}{t}\frac{E}{3\,(1-2\nu)}} \ .$$

The second term in the energy balance arises from considering the elastic strain according to the linear elastic stress-strain relationship. To verify Equation 7, thin sheets of gelatine ranging from 400–480 μm in thickness, were sandwiched between an acrylic sheet and acrylic disks with diameters ranging from approximately 0.5–4 cm [36].

7 Appendix C

Peeling a thin elastic film from a rigid substrate

For peeling a thin elastic layer of thickness t and width b from a rigid substrate, a partially separated state is considered in which a distance c is already peeled. The energy balance for creating distance Δc of new surface is then considered (illustrated in Figure 2). Assuming that the attached portion of the film is inextensible, the elastic energy, U_E, in the detached portion of the film is given by:

$$U_E = U_B - \frac{F^2 c}{2btE} \ , \tag{36}$$

where U_B is the elastic energy stored in the sharp bend of the film, and the second term is the elastic energy stored in stretching the detached portion of the film. The surface energy, U_S, is given by:

$$U_S = -cb\gamma \ . \tag{37}$$

The potential energy term is the sum of the work done by the force in **x** and in **y**, and can be derived by trigonometry. Given that the force is applied at an angle of θ to the substrate surface, the **x** and **y** components of the force are $F\cos\theta$ and $F\sin\theta$, respectively. The distance travelled by the force in **x** and **y** is given by:

$$\Delta x = \Delta c + c\cos\theta - (c + \Delta c)\cos\theta = \Delta c\,(1 - \cos\theta) \ , \tag{38}$$

$$\Delta y = (c + \Delta c)\sin\theta - c\sin\theta = \Delta c \sin\theta \ . \tag{39}$$

The work done by the force in propagating the crack a distance Δc is the sum of the work done in **x** and **y**, giving:

$$U_P = F\sin\theta\Delta c\sin\theta - F\cos\theta\Delta c\,(1 - \cos\theta) \ , \tag{40}$$

$$U_P = F\Delta c\left(1 - \cos^2\theta\right) - F\Delta c\left(\cos\theta - \cos^2\theta\right) \ , \tag{41}$$

$$U_P = F\Delta c\,(1 - \cos\theta) \ . \tag{42}$$

It is important to note here that Kendall does not consider the additional movement in the applied force owing to elastic extension of the film. However, Kendall states that the elastic term can be neglected for most materials, unless stresses up to $10E$ can be sustained before failure, or when the peel angle becomes small.

The total energy, U_T, is then given by:

$$U_T = -cb\gamma + Fc\,(1 - \cos\theta) + U_B + \frac{F^2 c}{2btE} = 0 \ . \tag{43}$$

From this, the peeling force can be found for three scenarios: (1) considering only surface and potential energies, F_{surf}, (2) considering only elastic and potential energies, $F_{elastic}$, and (3) considering all energies, F_{total}, summarised in the following:

$$\frac{\delta U_T}{\delta c} = -b\gamma + F\left(1-\cos\theta\right) + \frac{F^2}{2btE} = 0 \ , \tag{44}$$

$$F_{surf} = \frac{b\gamma}{1-\cos\theta} \ , \tag{45}$$

$$F_{elastic} = b\sqrt{2Et\gamma} \ , \tag{46}$$

$$0 = \left(\frac{F_{total}}{b}\right)^2 \frac{1}{2tE} + \left(\frac{F_{total}}{b}\right)\left(1-\cos\theta\right) - \gamma \ . \tag{47}$$

8 Appendix D

Contact-splitting theory

Starting with the adhesive force from JKR theory [33], we can say that as the substrate radius, R_2, approaches infinity (i.e. essentially a flat substrate), R^* becomes the radius of the top sphere, R_1, which we will now refer to as R_0. The adhesive force, F_0, for a single spherical contact is then given by:

$$F_0 = \frac{3}{2}\gamma\pi R_0 \ . \tag{48}$$

If we divide the contact into an array of n contacts with radius, R, given by:

$$R = \frac{R_0}{\sqrt{n}} \ , \tag{49}$$

so that the contact area of the array, $n\pi R^2$, is equal to that of the single contact, πR_0^2. The adhesive force, F, for a contact is given by:

$$F = \frac{3}{2}\gamma\pi\left(\frac{R_0}{\sqrt{n}}\right) \ , \tag{50}$$

$$F = \frac{1}{\sqrt{n}}F_0 \ . \tag{51}$$

The total adhesive force for the array of spheres, F_T, can be found by summing over n to give:

$$F_T = \frac{n}{\sqrt{n}} F_0 \ , \tag{52}$$

which is identical to Equation 13, repeated below:

$$F_T = \sqrt{n} F_0 \ .$$

9 Appendix E

Contact-splitting theory can be used to estimate how the adhesive force ratio varies with the geometric parameters of areal density, ρ, geometric area, A, and fibre radius, R [68]. The number of pillars in the array, n, is given by:

$$n = \frac{\rho R_0^2}{r^2} \ . \tag{53}$$

For a spherically terminated pillar with self-similar scaling the total force scales with $\sqrt{n}$, giving the following adhesive force ratio:

$$\frac{F_T}{F_0} = \rho \sqrt{n} \ , \tag{54}$$

$$\frac{F_T}{F_0} = \rho^{\frac{3}{2}} R_0 r^{-1} \ . \tag{55}$$

Similarly, for curvature invariance the total force scales linearly with n, giving:

$$\frac{F_T}{F_0} = \rho n \ , \tag{56}$$

$$\frac{F_T}{F_0} = \rho^2 R_0^2 r^{-2} \ . \tag{57}$$

For a flat-ended, rigid punch we recall that the force scales with $n^{0.25}$, which gives:

$$\frac{F_T}{F_0} = \rho n^{\frac{1}{4}} \ , \tag{58}$$

$$\frac{F_T}{F_0} = \rho \left(\frac{\rho R_0^2}{r^2} \right)^{\frac{1}{4}} \ , \tag{59}$$

$$\frac{F_T}{F_0} = \rho^{\frac{5}{4}} R_0^{0.5} r^{-0.5} \ . \tag{60}$$